NANO LETTERS
Cite This: Nano Lett. XXXX, XXX, XXX−XXX
Letter
pubs.acs.org/NanoLett

Anapoles in Free-Standing III−V Nanodisks Enhancing Second-Harmonic Generation

Maria Timofeeva,*[,†] Lukas Lang,[†] Flavia Timpu,[†] Claude Renaut,[†] Alexei Bouravleuv,[‡] Igor Shtrom,[‡] George Cirlin,[§] and Rachel Grange*[,†]

[†]ETH Zurich, Optical Nanomaterial Group, Institute for Quantum Electronics, Department of Physics, Auguste-Piccard Hof 1, 8093 Zurich, Switzerland

[‡]Saint Petersburg Academic University, Ul. Khlopina 8/3, 194021 Saint Petersburg, Russia

[§]ITMO University, Kronverkskiy 49, 197101 Saint Petersburg, Russia

Supporting Information

ABSTRACT: Nonradiating electromagnetic configurations in nanostructures open new horizons for applications due to two essential features: a lack of energy losses and invisibility to the propagating electromagnetic field. Such radiationless configurations form a basis for new types of nanophotonic devices, in which a strong electromagnetic field confinement can be achieved together with lossless interactions between nearby components. In our work, we present a new design of free-standing disk nanoantennas with nonradiating current distributions for the optical near-infrared range. We show a novel approach to creating nanoantennas by slicing III−V nanowires into standing disks using focused ion-beam milling. We experimentally demonstrate the suppression of the far-field radiation and the associated strong enhancement of the second-harmonic generation from the disk nanoantennas. With a theoretical analysis of the electromagnetic field distribution using multipole expansions in both spherical and Cartesian coordinates, we confirm that the demonstrated nonradiating configurations are anapoles. We expect that the presented procedure of designing and producing disk nanoantennas from nanowires becomes one of the standard approaches to fabricating controlled chains of standing nanodisks with different designs and configurations. These chains can be essential building blocks for new types of lasers and sensors with low power consumption.

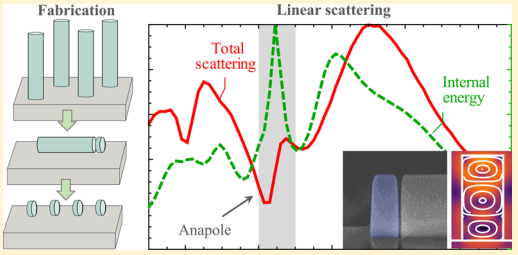

KEYWORDS: *III−V nanowires, second-harmonic generation, nonradiating electromagnetic configurations, anapole, disk nanoantennas, free-standing disks, focused ion-beam milling*

The concept of radiationless electromagnetic configurations, which are dark and not detectable in the far field, is still a significant theoretical and experimental challenge. These nonradiating configurations arise as a result of the destructive interference in the far-field between the radiation originating from two or more distinct current distributions inside the nanostructure.[1,2] In the past few years, significant results have been achieved in the theoretical analysis[3−6] and experimental demonstration[7,8] of anapole-type nonradiating current distributions. Initially, the term anapole was introduced in particle physics and then was used to describe dark matter in the universe.[9] In electrodynamics, first-order anapoles are nonradiating current distributions[10] in which electric and toroidal dipole moments[11−13] destructively interfere in the far field due to their identical radiation patterns,[1,14] which results in the suppression of the far-field radiation. The excitation of anapole modes in nanostructures provides a key possibility for the development of nonscattering metamaterials with strong electromagnetic field confinement inside.[15−17] This strong field confinement leads to a substantial increase of the nonlinear optical response, which can be employed both to detect anapoles and to design efficient nonlinear devices with low energy losses.

For the optical domain, the anapoles and toroidal modes were recently employed to enhance the third-order nonlinear optical effects in Ge disk nanoantennas[8,18] and were demonstrated in Si nanodisks.[7] In the microwave domain, dynamic anapoles were demonstrated experimentally and showed great potential for anapole applications in new types of metamaterials.[11,15,19] The concept of anapoles was utilized to design a new type of laser based on InGaAs disk nanoantennas, which can be an ideal coherent light source for optics at the nanoscale due to the absence of losses and low power consumption.[20] The reduction of energy radiation and invisibility to the propagating electromagnetic field make anapoles an essential basis for a new type of devices with lossless interactions between nearby components. Anapoles address the fundamental trade-off between the electromagnetic field confinement and energy dissipation, but a central

Received: February 28, 2018
Revised: May 4, 2018
Published: May 17, 2018

DOI: 10.1021/acs.nanolett.8b00830
Nano Lett. XXXX, XXX, XXX−XXX

challenge remains: how to create nanostructures that utilize anapoles effectively.

Our work is following the progressive research route[21−24] of nanoscale light manipulation with optically induced Mie resonances[15] in nanostructures from dielectric and semiconductor materials[25−27] with high refractive indexes as an alternative to plasmonic materials. This kind of nanostructure offer the possibility of reducing dissipative losses significantly and performing high resonance enhancement of electric and magnetic fields. In addition to these advantages, semiconductor materials can also be electrically doped and used for subwavelength active devices.[28−30] Furthermore, compared with the widely used silicon nanostructures, III−V materials such as GaAs, AlGaAs, or InAs, have direct band gaps and noncentrosymmetric structure, which make them promising materials for nonlinear photonic devices.

Here, we develop a new concept of vertically free-standing disk nanoantennas fabricated from epitaxially grown III−V nanowires sliced with focused ion beam milling. This technique offers unique opportunities for the fabrication of high-quality structures with variable radii, longitudinal heterostructures from lattice-mismatched materials with different refractive indexes,[31] and in crystal phases that are not available in bulk III−V materials.[32−35]

We experimentally show the lack of radiation in the near-infrared domain and the strong second-harmonic generation (SHG) enhancement due to an efficient electromagnetic field confinement. The multipole expansion of the electromagnetic field, performed in both spherical[7,36] and Cartesian coordinates,[37,38] shows that the fabricated standing disks have anapole-type nonradiating current distributions. Different from previous work using third-harmonic generation,[8] we demonstrated experimentally and theoretically how the anapole-type nonradiating current distributions lead to a strong enhancement of SHG at the position of the anapole. The proposed novel geometry of vertically free-standing disks has a lower aspect ratio between diameter and height compared with previous horizontally lying disk designs[7,8] and results in significant decrease in the substrate influence. This configuration, with new types of material based on III−V nanowires,[39] enables the use of any substrate regardless of the nanoantenna material and fabrication process. This is crucial for the development of nonlinear nanophotonic devices and for compatibility with complementary metal-oxide-semiconductor (CMOS) technologies.

We fabricated vertically standing disk nanoantennas from core−shell GaAs/AlGaAs nanowires (see the Methods section) in which AlGaAs and GaAs are noncentrosymmetric materials with strong second-order nonlinear optical properties.[40−42] Figure 1 presents the main steps of the fabrication process. We mechanically transferred nanowires, grown by molecular beam epitaxy,[43] onto a glass substrate covered with indium tin oxide (ITO) (Figure 1a). Using focused ion beam (FIB) milling, we sliced them into standing disks with diameters of 440 nm and heights of 210 nm. Application of the FIB milling technique allows us to create different configurations of nanoantennas, with improved quality of the sidewalls in comparison with lithography and etching methods. Nanowires can be transferred on any type of substrates (for example, transparent or silicon ones). Using the FIB slicing technique, we can easily get different configurations of chains of nanodisks. Scanning electron microscopy (SEM) images of the disk during fabrication are shown in Figure 1b,c. These SEM images are

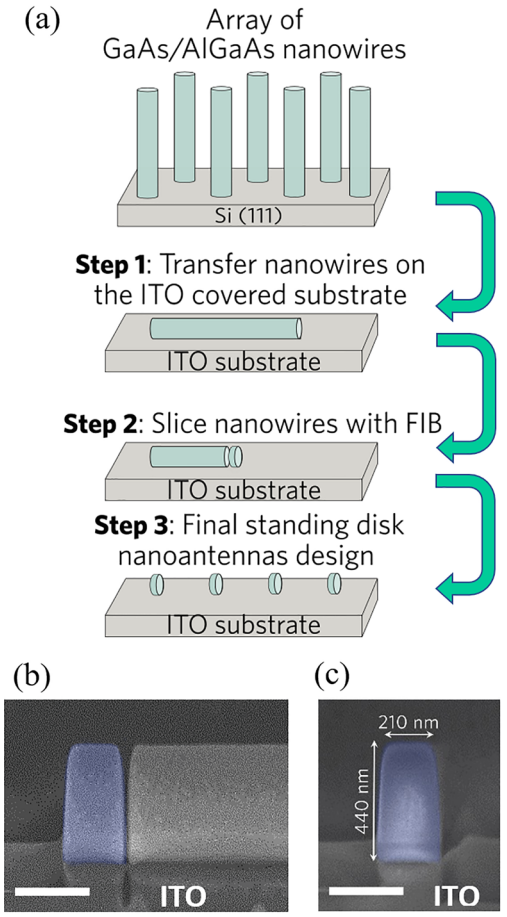

Figure 1. (a) Fabrication process flow using focused ion beam (FIB) milling for slicing the nanowires, placed on an indium tin oxide (ITO) substrate. (b) Scanning electron microscopy (SEM) image of one nanowire sliced by FIB into standing disks (highlighted in blue). (c) SEM image of the resulting single standing disk (blue) on an ITO substrate. Scale bars are 300 nm.

a side view of the ITO substrate with the nanowires. Additional SEM images illustrating the fabrication of disk nanoantennas are presented in Figure S2.

To demonstrate the ability of our design to support nonradiating current distributions, we developed a finite element method (FEM) model and studied two types of disk orientations on the glass substrate: vertically standing and horizontally lying disks, shown in Figure 2. The FEM simulations were performed using the COMSOL Multiphysics software. Our model considers a spherical system in which the disk nanoantenna is placed in the center of the sphere, as shown in Figure S1. The numerical aperture (NA) of the collection objective was accounted for by integrating the scattered signal over a limited solid angle (see Figure S1).

In contrast to horizontally lying disks[7,18,44] (Figure 2a), the vertically standing configuration (Figure 2d,g) is sensitive to the polarization of the incident electric field $\vec{E}$. Therefore, we considered two electric field directions: perpendicular (Figure 2d) and parallel (Figure 2g) to the disk. Figure 2b,e,h presents the simulated normalized scattering cross-sections for the corresponding orientations. These spectra were calculated both for a collection of the signal over the full sphere (red lines, Figure 2b,e,h) and via an objective with NA = 0.55 (blue lines, Figure 2b,e,h). All charts show the normalized internal electric

DOI: 10.1021/acs.nanolett.8b00830
Nano Lett. XXXX, XXX, XXX−XXX

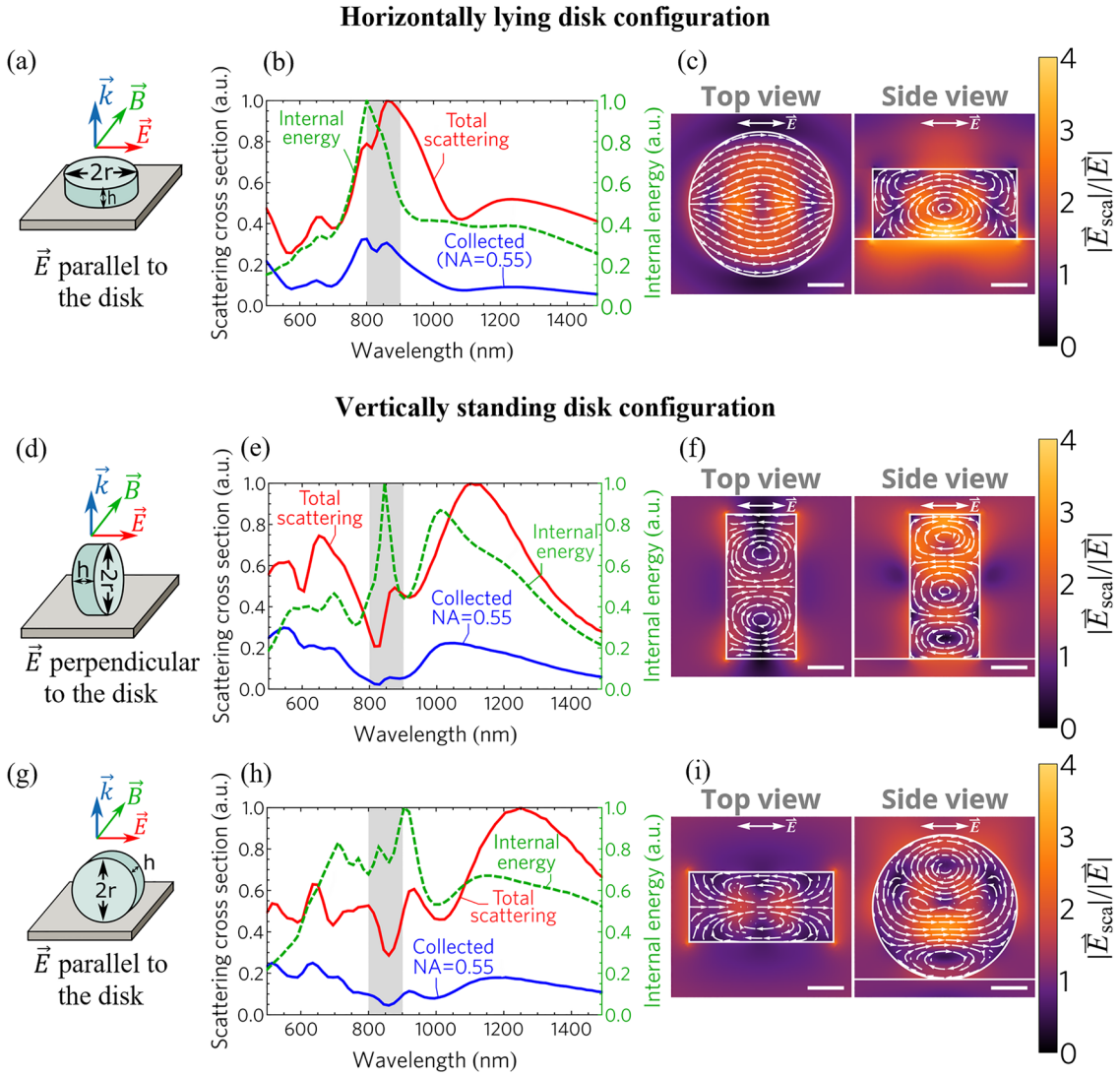

Figure 2. Horizontally lying disk configuration with (a) a schematic, in which vectors $\vec{k}$, $\vec{E}$, and $\vec{B}$ illustrate the directions of the wave vector, electric and magnetic fields, respectively; (b) a simulated scattering cross-section for the full-sphere collection of the signal (red lines), with collection via objective with numerical aperture (NA = 0.55) and corresponding internal electric energy; and (c) top and side views for electric field distributions, in which the scale is 100 nm and $\vec{E}_{sca}$ is the scattered electric field. Vertically standing disk configuration perpendicular to the incoming electric field with (d) the corresponding schematic, (e) simulation results, and (f) electric field distributions. Vertically standing disk configuration parallel to the incoming electric field with (g) the corresponding schematic, (h) simulation results, and (i) electric field distributions. The gray areas in panels b, e, and h highlight the wavelength region of interest.

energies, shown with green lines in Figure 2b,e,h. The results of the simulations demonstrate an important feature of the designed standing disks: the regions of the nonradiating current distributions are highly overlapping for both polarizations of the incoming electric field. Therefore, they will appear for unpolarized and arbitrarily polarized light as well. In our simulations, we are also taking into account the absorption of the material with values for real and imaginary parts of the refractive indices of GaAs and $Al_{0.3}Ga_{0.7}As$.[45]

The scattering cross-section spectra from the vertically standing disks for both polarizations (red lines, Figure 2e,h) display sharp drops accompanied by the corresponding peaks of the internal electric energy (green lines, Figure 2e,h) between 800 and 900 nm (highlighted gray regions in Figure 2). This demonstrates an efficient electromagnetic field confinement with suppressed far-field scattering, indicating nonradiating current distributions.[1,7] We are not considering the other drops in the scattering spectra because they are not accompanied by internal energy peaks. While the horizontally lying disk is the standard geometry for disk nanoantennas,[7,18,44] the nonradiating configurations in such structures appear only for high aspect ratios, around 4:1 for Si[7] and Ge.[8,18] In our geometry, the nonradiating configurations appear for an aspect ratio of 2:1, as shown on SEM image Figure 1c.

We calculated the electric field distributions inside the disks, and we present the images for the corresponding results for the wavelengths of the internal energy peak in the region 800−900 nm in Figure 2c,f,i. All images of the electric field distributions are shown in the plane that corresponds to the direction of $\vec{E}$ shown on each image, and all cross-sections were taken through the center of the disk. The toroidal current distributions, shown in panels f and i of Figure 2, indicate the presence of the toroidal mode inside the vertically standing nanoantennas.[1]

To demonstrate experimentally the nonradiating current distribution in the fabricated vertically standing disks in the region 800−900 nm, we measured the linear and nonlinear

DOI: 10.1021/acs.nanolett.8b00830
Nano Lett. XXXX, XXX, XXX−XXX

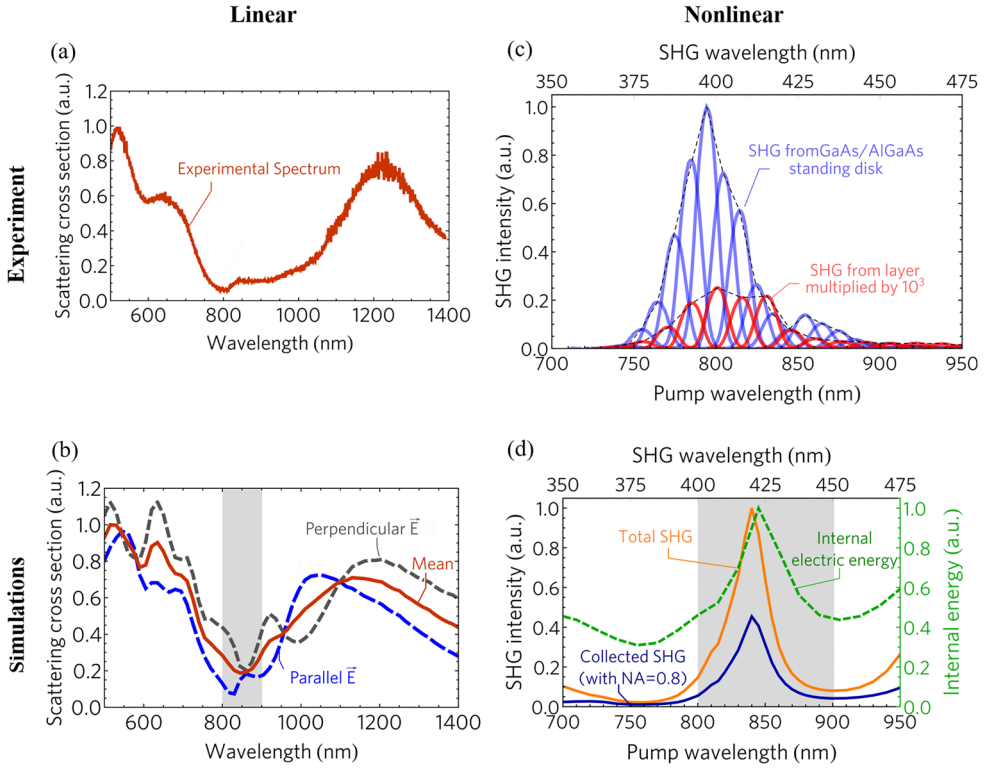

Figure 3. (a) Experimentally measured scattering cross-section of an GaAs/AlGaAs disk nanoantenna. (b) Simulated scattering cross-section spectra for both parallel (blue dashed line) and perpendicular (dashed gray line) polarizations of the incoming electric field and the average over both polarizations (solid red line). (c) Fundamental wavelength dependence of the SHG spectra of the GaAs/AlGaAs disk (blue lines) and epitaxial layer (red lines, signals were multiplied by 10^3); the dashed gray lines are the envelope of the SHG spectra, and SHG spectra were recorded by sweeping the excitation laser wavelength from 690 to 900 nm with steps of 10 nm. (d) Simulated SHG signal for the full sphere collection (orange line), collection via objective with numerical aperture 0.8 (blue line), and the internal electric energy of the fundamental radiation (dashed green line). The gray areas in panels b and d highlight the regions of interest.

optical responses. Figure 3a displays the scattering cross-section from a single standing disk (Figure 1c) measured in a dark-field spectroscopy setup (see section 3.2 in the Supporting Information). Figure 3b shows the corresponding linear scattering cross-section averaged over two polarizations calculated with the FEM model. The simulated linear scattering cross-section matches the experimental one, presented in Figure 3a,b, reproducing all major features.

The strong confinement of the electric field inside the vertically standing disks, demonstrated in numerical simulations (Figure 2f,i for the region 800−900 nm), leads to a resonant enhancement of the SHG. We demonstrate this enhancement by measuring the SHG intensity spectra from the standing disk (blue lines, Figure 3c) and comparing them with the SHG spectra from an epitaxially grown layer of AlGaAs (red lines, Figure 3c). The total SHG enhancement factor of the standing disk is around 5×10^3 in comparison to the layer (see section 3.4 of the Supporting Information). To analyze the SHG in the fabricated standing disks, we extended the FEM model with the corresponding SHG simulations (see section 1.1 of the Supporting Information), and Figure 3d presents the results of these SHG simulations. The small red shifts between experimental and simulated SHG spectra could arise from deviations of shape and dimensions during the fabrication process in comparison to the perfect disk geometry in the FEM model. Following the work in ref 46, we estimate the conversion efficiency of the SHG from the studied GaAs/AlGaAs disk nanoantennas at the position of the maximum (Figure 3c,d) to be 1.9×10^{-5} for an incident intensity of 1 GW/cm^2.

To show that the chosen geometry and aspect ratio parameters are optimal for the highest enhancement of the SHG at the anapole mode, we performed calculations for different sizes and aspect ratios of the disks. The corresponding results are presented in section 4 in the Supporting Information.

Simultaneous implementation of the multipole expansion of the electromagnetic field in spherical and Cartesian coordinates lets us unambiguously determine the nature of the nonradiating current distributions in the studied free-standing disks. In spherical coordinates, the far-field radiation can be easily decomposed up to higher-order multipoles. However, the toroidal multipoles share the same radiation pattern as the corresponding electric multipoles,[1] which makes them indistinguishable in spherical coordinates, while the Cartesian expansion separates them (section 2 of the Supporting Information).

For the spherical multipole expansion,[36] we evaluated the contributions from electric (ED_{sph}) and magnetic (MD_{sph}) dipoles, electric (EQ_{sph}) and magnetic (MQ_{sph}) quadrupoles, and electric (EO_{sph}) and magnetic (MO_{sph}) octupoles (Figure 4a,c). The sum of these individual contributions, shown with red lines in Figure 4a,c, matches the calculated scattering cross-section for the standing disk, shown with the red lines in Figure 2e. As we can see from the spherical multipole expansions, the contributions from the spherical octupoles are negligible, which allows us to perform the Cartesian multipole expansion up to

DOI: 10.1021/acs.nanolett.8b00830
Nano Lett. XXXX, XXX, XXX−XXX

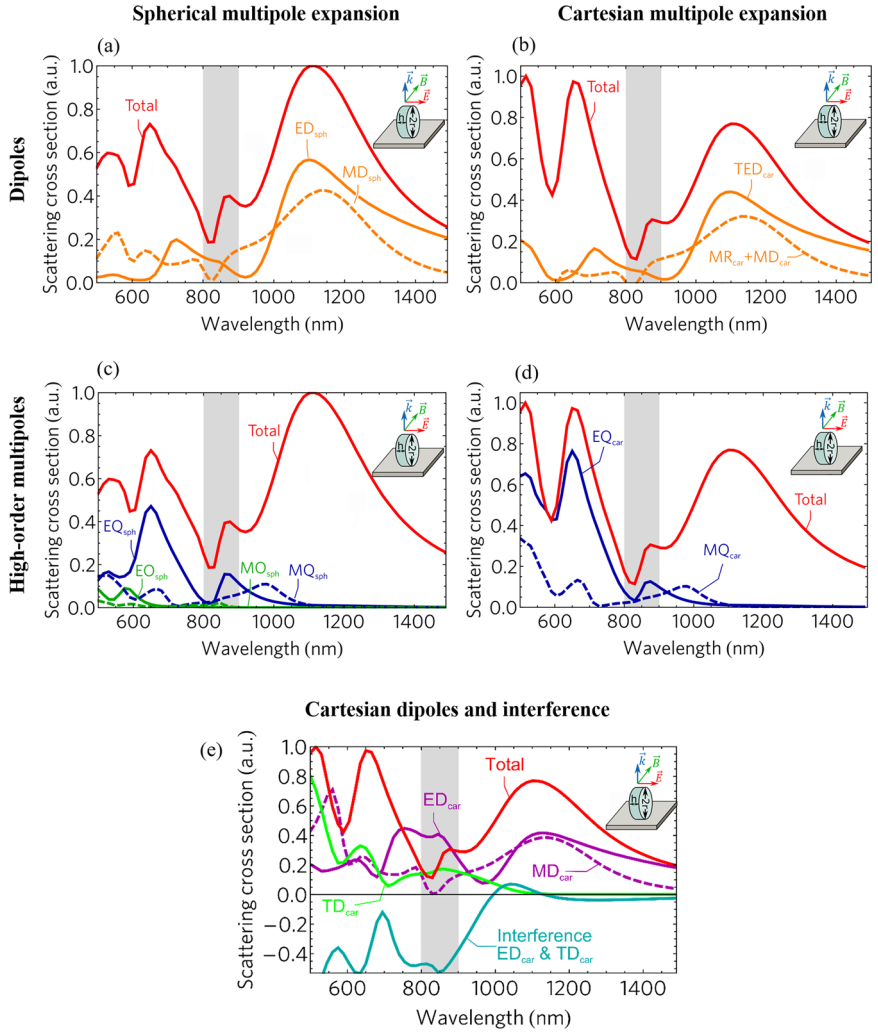

Figure 4. Geometry schematic for all charts is the same and presented on the insets. (a) Contributions from spherical electric ED_{sph} and magnetic MD_{sph} dipoles to the total scattering intensity (red line). (b) Contributions from Cartesian total electric dipole TED_{car} and total magnetic dipole TMD_{sph} (neglecting the mean square radius correction) to the total scattering intensity (red line). (c) Contributions from spherical electric EQ_{sph} and magnetic MQ_{sph} quadrupoles and electric EO_{sph} and magnetic MO_{sph} octupoles to the total scattering intensity. (d) Contributions from Cartesian electric EQ_{sph} and magnetic MQ_{sph} quadrupoles. (e) Cartesian electric (ED_{car}) and magnetic (MD_{car}) dipoles, toroidal electric dipole (TD_{car}), and interference terms of ED_{car} and TD_{car} (see equations S10 and S11 in the Supporting Information) to the total scattering cross-section (red line). The negative value of the interference term (cyan line) arises because it is only part of the physical contribution of the total electric dipole TED_{car}.

electric and magnetic quadrupoles terms only.[37,38] The corresponding expressions for the Cartesian multipoles contributions are presented in Table S1.

The equation for the total scattering intensity for the Cartesian multipole expansion is presented in the eqs S10−11 in the Supporting Information. The total electric dipole contribution (TED_{car}) contains the electric (ED_{car}) and toroidal (TD_{car}) dipoles shown in purple and green lines in Figure 4e, together with their interferences that are shown with the blue line in the Figure 4e. The TED_{car} equals the electric dipole in the spherical coordinates (ED_{sph}).[3,36] The contribution from Cartesian magnetic dipole (MD_{car}) is shown with a purple dashed line in Figure 4e. The sum of the Cartesian magnetic dipole (MD_{car}) and interference term (eqs S10−11) with its mean square radius (MR_{car}) is shown with a dashed orange line in Figure 4b and corresponds to the magnetic dipole (MD_{sph}) in spherical coordinates. The last two terms in eq S1 are the contributions from the electric (EQ_{car}) and magnetic (MQ_{car}) quadrupoles that are represented with solid and dashed blue lines in Figure 4d. The differences in the short wavelength range for the total sum of spherical and Cartesian multipoles expansions, shown in red in Figure 4a−d, are coming from the orders of the contributions that we are considering. For the spherical multipole expansion, we are including contributions up to octupole terms, while for the Cartesian multipole expansion, we are taking contributions up to the order of $1/r^5$, and this does not affect the anapole range in which octupole contributions are negligible (see Figure 4).

The spherical multipole expansion (Figure 4a,c) shows that the region with the drop of the total scattering cross-section (800−900 nm) has a non-negligible contribution only from the electric dipole ED_{sph}, while others are suppressed. The decomposition into Cartesian multipoles demonstrates high values of electric (ED_{car}) and toroidal dipoles (TD_{car}) in this region together with a strong destructive interference between them (Figure 4e).[4,37,38] The other multipoles, including the magnetic dipole (MD_{car}), in the Cartesian representation have no contributions in this region (Figure 4d,e). The multipole

DOI: 10.1021/acs.nanolett.8b00830
Nano Lett. XXXX, XXX, XXX−XXX

expansion demonstrates the destructive interference between electric and toroidal dipoles and the simultaneous suppression of the higher-order multipoles. While the interference between the electric and toroidal dipole is not totally destructive at the position of the minimum, the main contribution to the internal current distributions is clearly not radiating into the far field. Therefore, our theoretical analysis shows the anapole nature of nonradiating current distributions in the designed and experimentally studied vertically standing disk nanoantennas.

In summary, we have presented a new design concept of nanoantennas based on free-standing disks, a novel procedure for fabricating them from III−V nanowires, and an end-to-end approach, from theory to experiment, with which to study nanostructures supporting nonradiating configurations in the optical range. The presented method of slicing nanowires with FIB milling allows us to create disk-based configurations on any substrate. This method significantly expands the possible application area of III−V disk nanoantennas. The approach of FIB nanowire slicing allows us to easily create nanoantenna chains of different designs[26,47] without relying on the substrate material and to make them compatible with CMOS technologies. This method, presented in our work, is general and could be utilized for different types of nanowires and nanomaterials.

The presented end-to-end approach includes a numerical simulation with analysis of the multipole expansion of the electric field and experimental demonstration of nonradiating current distributions by linear scattering and SHG spectra measurements. We applied it for an experimental and theoretical demonstration of nonradiating anapoles in the geometry of vertically standing III−V nanodisks.

In the near future, we expect that the developed procedure of nanowires slicing can create a new branch of nanotechnology to fabricate controlled chains of standing nanodisks with different designs and configurations. Such type of nanoantennas' chains could be a core element for lasers and sensors[48,49] with low power consumption based on lossless nonlinear nanophotonic components supporting anapoles and compatible with CMOS technologies.

Methods. *Fabrication of GaAs/AlGaAs Disks.* The vertically standing nanodisks were fabricated from GaAs/AlGaAs core−shell nanowires deposited on ITO glass substrate using FIB milling. The nanowires were grown by molecular-beam epitaxy on Si (111) substrates using Au colloid droplets as a catalyst material.[43] As the first step, the GaAs core of nanowires were grown, and then, in situ, the $Al_{0.2}Ga_{0.8}As$ shells were grown to passivate the surface states.[50] Next, nanowires were transferred on the ITO-covered glass substrate. After that, we used a focused gallium liquid metal ion microscope coupled with a high-resolution field effect gun scanning electron microscope, (NVision 40, Carl Zeiss AG). The system is equipped with a proprietary nanopatterning software (NPVE, NanoPatterning and Visualization Engine, Carl Zeiss AG). The software can control the focused-ion-beam and the electron-beam microscopes. We can capture images of the desired nanowires with the electron microscope and then create a layout with the NPVE software on the SEM image. Later, we run this layout to mill our nanowires with the focused ion beam and produce the nanowire-based antennas.

Far-Field Linear Spectroscopy. The characterization of linear-scattering cross-sections were performed in a dark-field spectroscopy setup[51] (section 3.1 of the Supporting Information). The nanoantenna sample was irradiated with a halogen lamp source. The scattered light was collected in a transmission geometry using a 50× objective with a numerical aperture of NA = 0.55.

Nonlinear Optical Characterization. Nonlinear optical measurements of the SHG spectra were performed with a nonscanning transmission optical microscope (Figure S4). For the excitation of the samples, we used a tunable Ti:sapphire laser (in the range 690−900 nm with steps of 10 nm). The laser light was focused with a 10× objective on the ITO-covered glass with isolated disk nanoantennas. The signal was then collected with a 100× objective (NA= 0.8) and focused onto a scientific CMOS camera and on the spectrometer. The polarization of the excitation laser was fixed at the same value for all steps. As a reference sample for the determination of the enhancement factor, we measured the SHG spectra from an epitaxially grown layer of AlGaAs with a thickness of 800 nm. The corresponding spectra from the layer and the disks were normalized by the effective volume of the measured structures and the differences in the setup parameters for reflection and transmission measurements (section 3.3 of the Supporting Information). We also measured the dependence of the SHG signal intensity for different incident power and observed a typical quadratic response (Figure S5).

Numerical FEM Simulations. The numerical simulations were performed using the COMSOL Multiphysics software package. For the numerical simulations of the scattering cross-section from the disk structures, we developed a model to calculate the linear-scattering cross-section from the disk nanoantennas and the spectra of SHG for different geometries. In our numerical model, we calculate how much is collected in the far field by considering the numerical aperture (NA) of the collection objective. The collected signal is shown with blue lines in Figure 2; moreover, in Figure S1, we highlight the solid angle that is collected experimentally (blue portion of the spheres, "numerical aperture"). For the linear-scattering measurements, we are using a 50× objective with NA = 0.55. For the nonlinear responses, we are using a 100× objective with NA = 0.8, and both the collected (blue) and total (orange) SHG intensities are shown in Figure 3d.

Multipole Expansions. Multipole expansions were performed in both the spherical and the Cartesian coordinate systems. We analyze the contributions to the total scattering cross-section from the individual multipoles up to octupoles terms in spherical coordinates and up to the order of $\frac{1}{r^5}$ for Cartesian ones.[38] The spherical and Cartesian multipole expansions were implemented in the developed COMSOL model (section 2 of the Supporting Information).

■ ASSOCIATED CONTENT

Supporting Information

The Supporting Information is available free of charge on the ACS Publications website at DOI: 10.1021/acs.nanolett.8b00830.

Details about experimental methods and theoretical analysis with multipole expansions in spherical and Cartesian coordinates, numerical simulations of SHG, numerical COMSOL models for multipole expansions in spherical and Cartesian coordinates, and experimental setups for linear and nonlinear characterizations. (PDF)

DOI: 10.1021/acs.nanolett.8b00830
Nano Lett. XXXX, XXX, XXX−XXX

AUTHOR INFORMATION

Corresponding Authors

*E-mail: mtimo@phys.ethz.ch.
*E-mail: grange@phys.ethz.ch.

ORCID

Maria Timofeeva: 0000-0001-7192-8322
Flavia Timpu: 0000-0002-0951-4070
Alexei Bouravleuv: 0000-0002-7432-2091

Author Contributions

The manuscript was written through contributions of all authors. R.G. designed the experiment. M.T. did the nano-antenna design, second-harmonic-generation experiments, data analysis, theoretical modeling, and manuscript writing. L.L. performed the second-harmonic-generation measurements, numerical simulations, and theoretical analysis. F.T. performed the linear optical characterization and helped with numerical simulations. C.R. did the focused-ion-beam milling of nanowires and characterization with scanning electron microscopy. A.B., I.S., and G.C. fabricated the nanowires with molecular-beam epitaxy. All authors have given approval to the final version.

Notes

The authors declare no competing financial interest.

ACKNOWLEDGMENTS

The authors thank the Scientific Centre for Optical and Electron Microscopy (ScopeM) of ETH Zurich, financial support from the Swiss National Science Foundation (SNF) (grant no. 150609), bridge project no. 173829, and the ERC starting grant Chi2-Nano-Oxide. The nanowire samples were grown under the support of the Russian Science Foundation (RSF) project no. 14-12-00393.

ABBREVIATIONS

Si, silicon; Ge, germanium; InGaAs, indium gallium arsenide; GaAs, gallium arsenide; AlGaAs, aluminum gallium arsenide, InAs, indium arsenide; CMOS, complementary metal oxide semiconductor; SHG, second-harmonic generation; ITO, indium tin oxide; FIB, focused ion beam; SEM, scanning electron microscopy; FEM, finite element model; NA, numerical aperture; ED_{sph}, spherical electric dipole; MD_{sph}, spherical magnetic dipole; EQ_{sph}, spherical electric quadrupole; MQ_{sph}, spherical magnetic quadrupole; EO_{sph}, spherical magnetic octupole; MO_{sph}, spherical magnetic octupole; TED_{car}, Cartesian total electric dipole contribution; ED_{car}, Cartesian electric dipole; TD_{car}, toroidal dipole; MD_{car}, Cartesian magnetic dipole; MR_{car}, mean square radius; EQ_{car}, Cartesian electric quadrupole; MQ_{car}, Cartesian magnetic quadrupole

REFERENCES

(1) Papasimakis, N.; Fedotov, V. A.; Savinov, V.; Raybould, T. A.; Zheludev, N. I. Electromagnetic Toroidal Excitations in Matter and Free Space. *Nat. Mater.* **2016**, *15* (3), 263−271.

(2) Kruk, S.; Kivshar, Y. Functional Meta-Optics and Nanophotonics Govern by Mie Resonances. *ACS Photonics* **2017**, *4* (11), 2638−2649.

(3) Evlyukhin, A. B.; Fischer, T.; Reinhardt, C.; Chichkov, B. N. Optical Theorem and Multipole Scattering of Light by Arbitrarily Shaped Nanoparticles. *Phys. Rev. B: Condens. Matter Mater. Phys.* **2016**, *94* (20), 1−7.

(4) Raybould, T.; Fedotov, V. A.; Papasimakis, N.; Youngs, I.; Zheludev, N. I. Exciting Dynamic Anapoles with Electromagnetic Doughnut Pulses. *Appl. Phys. Lett.* **2017**, *111* (8), 081104.

(5) Luk'yanchuk, B.; Paniagua-Domínguez, R.; Kuznetsov, A. I.; Miroshnichenko, A. E.; Kivshar, Y. S. Hybrid Anapole Modes of High-Index Dielectric Nanoparticles. *Phys. Rev. A: At., Mol., Opt. Phys.* **2017**, *95* (6), 1−8.

(6) Luk'yanchuk, B.; Paniagua-Domínguez, R.; Kuznetsov, A. I.; Miroshnichenko, A. E.; Kivshar, Y. S. Suppression of Scattering for Small Dielectric Particles: Anapole Mode and Invisibility. *Philos. Trans. R. Soc., A* **2017**, *375* (2090), 20160069.

(7) Miroshnichenko, A. E.; Evlyukhin, A. B.; Yu, Y. F.; Bakker, R. M.; Chipouline, A.; Kuznetsov, A. I.; Luk'yanchuk, B.; Chichkov, B. N.; Kivshar, Y. S. Nonradiating Anapole Modes in Dielectric Nanoparticles. *Nat. Commun.* **2015**, *6*, 1−8.

(8) Grinblat, G.; Li, Y.; Nielsen, M. P.; Oulton, R. F.; Maier, S. A. Enhanced Third Harmonic Generation in Single Germanium Nanodisks Excited at the Anapole Mode. *Nano Lett.* **2016**, *16*, 4635−4640.

(9) Zel'dovich, I. B. Electromagnetic Interaction with Parity Violation. *J. Exptl. Theor. Phys.* **1957**, *33*, 1531−1533.

(10) Devaney, A. J.; Wolf, E. Radiating and Nonradiating Classical Current Distributions and the Fields They Generate. *Phys. Rev. D: Part. Fields* **1973**, *8* (4), 1044−1047.

(11) Kaelberer, T.; Fedotov, V. A.; Papasimakis, N.; Tsai, D. P.; Zheludev, N. I. Toroidal Dipolar Response in a Metamaterial. *Science (Washington, DC, U. S.)* **2010**, *330* (6010), 1510−1512.

(12) Savinov, V.; Fedotov, V. A.; Zheludev, N. I. Toroidal Dipolar Excitation and Macroscopic Electromagnetic Properties of Metamaterials. *Phys. Rev. B: Condens. Matter Mater. Phys.* **2014**, *89* (20), 1 DOI: 10.1103/PhysRevB.89.205112.

(13) Basharin, A. A.; Kafesaki, M.; Economou, E. N.; Soukoulis, C. M.; Fedotov, V. A.; Savinov, V.; Zheludev, N. I. Dielectric Metamaterials with Toroidal Dipolar Response. *Phys. Rev. X* **2015**, *5* (1), 1−11.

(14) Afanasiev, G. N.; Stepanovsky, Y. P. The Electromagnetic Field of Elementary Time-Dependent Toroidal Sources. *J. Phys. A: Math. Gen.* **1995**, *28* (16), 4565−4580.

(15) Fedotov, V. A.; Rogacheva, A. V.; Savinov, V.; Tsai, D. P.; Zheludev, N. I. Resonant Transparency and Non-Trivial Non-Radiating Excitations in Toroidal Metamaterials. *Sci. Rep.* **2013**, *3*, 1−5.

(16) Gupta, M.; Savinov, V.; Xu, N.; Cong, L.; Dayal, G.; Wang, S.; Zhang, W.; Zheludev, N. I.; Singh, R. Sharp Toroidal Resonances in Planar Terahertz Metasurfaces. *Adv. Mater.* **2016**, *28*, 8206−8211.

(17) Gongora, J.; Gael, F.; Fratalocchi, A. Fundamental and High-Order Anapoles in All- Dielectric Metamaterials via Fano − Feshbach Modes Competition. *Nanotechnology* **2017**, *28*, 104001.

(18) Grinblat, G.; Li, Y.; Nielsen, M. P.; Oulton, R. F.; Maier, S. A. Efficient Third Harmonic Generation and Nonlinear Subwavelength Imaging at a Higher-Order Anapole Mode in a Single Germanium Nanodisk. *ACS Nano* **2017**, *11* (1), 953−960.

(19) Marinov, K.; Boardman, A. D.; Fedotov, V. A.; Zheludev, N. Toroidal Metamaterial. *New J. Phys.* **2007**, *9*, 324.

(20) Totero Gongora, J. S.; Miroshnichenko, A. E.; Kivshar, Y. S.; Fratalocchi, A. Anapole Nanolasers for Mode-Locking and Ultrafast Pulse Generation. *Nat. Commun.* **2017**, *8*, 15535.

(21) Staude, I.; Schilling, J. Metamaterial-Inspired Silicon Nanophotonics. *Nat. Photonics* **2017**, *11* (5), 274−284.

(22) Jahani, S.; Jacob, Z. All-Dielectric Metamaterials. *Nat. Nanotechnol.* **2016**, *11* (1), 23−36.

(23) Zhao, Q.; Zhou, J.; Zhang, F.; Lippens, D. Mie Resonance-Based Dielectric Metamaterials. *Mater. Today* **2009**, *12* (12), 60−69.

(24) Kivshar, Y.; Miroshnichenko, A. E. Meta-Optics with Mie Resonances. *Opt. Photonics News* **2017**, *28*, 24−31.

(25) Evlyukhin, A. B.; Reinhardt, C.; Seidel, A.; Luk'Yanchuk, B. S.; Chichkov, B. N. Optical Response Features of Si-Nanoparticle Arrays. *Phys. Rev. B: Condens. Matter Mater. Phys.* **2010**, *82* (4), 1−12.

DOI: 10.1021/acs.nanolett.8b00830
Nano Lett. XXXX, XXX, XXX−XXX

(26) Krasnok, A. E.; Miroshnichenko, A. E.; Belov, P. a.; Kivshar, Y. S. All-Dielectric Optical Nanoantennas. *Opt. Express* **2012**, *20* (18), 20599−20604.
(27) Valentine, J.; Li, J.; Zentgraf, T.; Bartal, G.; Zhang, X. An Optical Cloak Made of Dielectrics. *Nat. Mater.* **2009**, *8* (7), 568−571.
(28) Cao, L.; White, J. S.; Park, J.-S.; Schuller, J. A.; Clemens, B. M.; Brongersma, M. L. Engineering Light Absorption in Semiconductor Nanowire Devices. *Nat. Mater.* **2009**, *8* (8), 643−647.
(29) Garín, M.; Fenollosa, R.; Alcubilla, R.; Shi, L.; Marsal, L. F.; Meseguer, F. All-Silicon Spherical-Mie-Resonator Photodiode with Spectral Response in the Infrared Region. *Nat. Commun.* **2014**, *5*, 3440.
(30) Grzela, G.; Paniagua-Domínguez, R.; Barten, T.; Fontana, Y.; Sánchez-Gil, J. A.; Gómez Rivas, J. Nanowire Antenna Emission. *Nano Lett.* **2012**, *12* (11), 5481−5486.
(31) Assali, S.; Van Dam, D.; Haverkort, J. E. M.; Bakkers, E. P. A. M. High Refractive Index in Wurtzite GaP Measured from Fabry-Pérot Resonances. *Appl. Phys. Lett.* **2016**, *108* (17), 173101.
(32) Dick, K. A.; Thelander, C.; Samuelson, L.; Caroff, P. Crystal Phase Engineering in Single InAs Nanowires. *Nano Lett.* **2010**, *10* (9), 3494−3499.
(33) Lehmann, S.; Jacobsson, D.; Dick, K. A. Crystal Phase Control in GaAs Nanowires : Opposing Trends in the Ga- and As-Limited Growth Regimes. *Nanotechnology* **2015**, *26* (30), 301001.
(34) Jacobsson, D.; Panciera, F.; Tersoff, J.; Reuter, M. C.; Lehmann, S.; Hofmann, S.; Dick, K. A.; Ross, F. M. Interface Dynamics and Crystal Phase Switching in GaAs Nanowires. *Nature* **2016**, *531* (7594), 317−322.
(35) Gudiksen, M. S.; Lauhon, L. J.; Wang, J.; Smith, D. C.; Lieber, C. M. Growth of Nanowire Superlattice Structures for Nanoscale Photonics and Electronics. *Nature* **2002**, *415*, 617−620.
(36) Grahn, P.; Shevchenko, A.; Kaivola, M. Electromagnetic Multipole Theory for Optical Nanomaterials. *New J. Phys.* **2012**, *14*, 93033.
(37) Radescu, E. E.; Vaman, G. Exact Calculation of the Angular Momentum Loss, Recoil Force, and Radiation Intensity for an Arbitrary Source in Terms of Electric, Magnetic, and Toroid Multipoles. *Phys. Rev. E: Stat. Phys., Plasmas, Fluids, Relat. Interdiscip. Top.* **2002**, *65* (4), 046609.
(38) Radescu, E., Jr.; Vaman, G. Cartesian Multipole Expansions and Tensorial Identities. *Prog. Electromagn. Res. B* **2012**, *36*, 89−111.
(39) Vukajlovic-Plestina, J.; Kim, W.; Dubrovski, V. G.; Tütüncüoğlu, G.; Lagier, M.; Potts, H.; Friedl, M.; Fontcuberta i Morral, A. Engineering the Size Distributions of Ordered GaAs Nanowires on Silicon. *Nano Lett.* **2017**, *17* (7), 4101−4108.
(40) Timofeeva, M.; Bouravleuv, A.; Cirlin, G.; Shtrom, I.; Soshnikov, I.; Reig Escale, M.; Sergeyev, A.; Grange, R. Polar Second-Harmonic Imaging to Resolve Pure and Mixed Crystal Phases Along GaAs Nanowires. *Nano Lett.* **2016**, *16*, 6290−6297.
(41) Liu, S.; Sinclair, M. B.; Saravi, S.; Keeler, G. A.; Yang, Y.; Reno, J.; Peake, G. M.; Setzpfandt, F.; Staude, I.; Pertsch, T.; et al. Resonantly Enhanced Second-Harmonic Generation Using III-V Semiconductor All-Dielectric Metasurfaces. *Nano Lett.* **2016**, *16* (9), 5426−5432.
(42) Grange, R.; Bronstrup, G.; Kiometzis, M.; Sergeyev, A.; Richter, J.; Leiterer, C.; Fritzsche, W.; Gutsche, C.; Lysov, A.; Prost, W.; et al. Far-Field Imaging for Direct Visualization of Light Interferences in GaAs Nanowires. *Nano Lett.* **2012**, *12* (10), 5412−5417.
(43) Bouravleuv, A. D.; Ilkiv, I.; Reznik, R.; Kotlyar, K.; Soshnikov, I. P.; Cirlin, G. E.; Brunkov, P.; Kirilenko, D.; Bondarenko, L.; Nepomnyaschiy, A.; et al. New Method for MBE Growth of GaAs Nanowires on Silicon Using Colloidal Au Nanoparticles. *Nanotechnology* **2018**, *29*, 045602.
(44) Wang, R.; Dal Negro, L. Engineering Non-Radiative Anapole Modes for Broadband Absorption Enhancement of Light. *Opt. Express* **2016**, *24* (17), 19048.
(45) Aspnes, D. E.; Kelso, S. M.; Logan, R. A.; Bhat, R. Optical Properties of AlxGa1-xAs. *J. Appl. Phys.* **1986**, *60* (2), 754−767.
(46) Gili, V. F.; Carletti, L.; Locatelli, A.; Rocco, D.; Finazzi, M.; Ghirardini, L.; Favero, I.; Gomez, C.; Lemaître, A.; Celebrano, M.; et al. Monolithic AlGaAs Second-Harmonic Nanoantennas. *Opt. Express* **2016**, *24* (14), 15965.
(47) Li, S. V.; Krasnok, A. E.; Lepeshov, S.; Savelev, R. S.; Baranov, D. G.; Alu, A. All-Optical Switching and Unidirectional Plasmon Launching with Electron-Hole Plasma Driven Silicon Nanoantennas. *Phys. Rev. Appl.* **2018**, *9* (1), 14015.
(48) Patolsky, F.; Zheng, G.; Lieber, C. M. Nanowire-Based Biosensors. *Anal. Chem.* **2006**, *78* (13), 4260.
(49) Patolsky, F.; Lieber, C. M. Nanowire Nanosensors. *Mater. Today* **2005**, *8* (4), 20−28.
(50) Demichel, O.; Heiss, M.; Bleuse, J.; Mariette, H.; Fontcuberta i Morral, I. A. Impact of Surfaces on the Optical Properties of GaAs Nanowires. *Appl. Phys. Lett.* **2010**, *97* (20), 201907.
(51) Timpu, F.; Hendricks, N. R.; Petrov, M.; Ni, S.; Renaut, C.; Wolf, H.; Isa, L.; Kivshar, Y.; Grange, R. Enhanced Second-Harmonic Generation from Sequential Capillarity- Assisted Particle Assembly of Hybrid Nanodimers. *Nano Lett.* **2017**, *17* (9), 5381−5388.

DOI: 10.1021/acs.nanolett.8b00830
Nano Lett. XXXX, XXX, XXX−XXX